HRR-PINN: A Deep Learning Method for Solving Complex Data-Driven Solutions

Huijuan Zhou[1,2] and Yong Chen[3,4*]

[1]*School of Science, Shanghai Maritime University, Shanghai 201306, China*
[2]*School of Mathematical Science, Shanghai Jiao Tong University, Shanghai 200240, China*
[3]*College of Mathematics and Systems Science, Shandong University of Science and Technology, Qingdao 266590, China*
[4]*School of Mathematical Sciences, Shanghai Key Laboratory of Pure Mathematics and Mathematical Practice, East China Normal University, Shanghai 200241, China*

(Received 14 February 2026; accepted manuscript online 12 March 2026)

Physics-informed neural networks (PINNs) have emerged as powerful tools for data-driven solutions of partial differential equations. However, when solving complex solutions with a sharp gradient or waveform mutation region, the traditional PINNs method frequently has significantly higher prediction errors in critical regions than in other areas because of randomly or uniformly distributed sampling points. To overcome the limitations of PINNs in solving complex solutions, we propose a high-residual region resampling PINN (HRR-PINN) method. The HRR-PINN method uses a two-stage paradigm. Pre-training focuses on global modeling to obtain the residual of the network training, which is helpful for achieving a more precise sampling optimization. Secondary training focuses on computational resources of critical regions to specialize in optimizing high-residual regions based on the global results of pretraining, that is, adding new points in high-residual regions and removing low-residual points from the original set. To illustrate the effectiveness of the HRR-PINN method, we applied it to single-periodic solutions, rogue wave solutions on single-periodic backgrounds, and double-periodic solutions of the second-type derivative nonlinear Schrödinger equation. Numerical experiments show that the HRR-PINN method significantly optimizes the distribution of sampling points and reduces prediction errors. This confirms the effectiveness for solving complex solutions with abrupt waveform changes or sharp gradients of the HRR-PINN method.

DOI: 10.1088/0256-307X/43/4/040003 CSTR: 32039.14.0256-307X.43.4.040003

1. Introduction. Physics-informed neural networks (PINNs), as an emerging method integrating data-driven learning and physical constraints, have become a powerful tool for solving forward-inverse problems of partial differential equations (PDEs).[1–10] The core concept of PINNs is to use a neural network to approximate the solution of the target equation while incorporating the residual of the physical equation into the loss function to achieve a dual-constraint training framework that combines data information and physical laws. The introduction of strong-form PDE constraints in neural networks implies that the selection of collocation points for calculating the PDE residuals is of crucial importance. In 2020, researchers demonstrated that the selection of internal collocation points significantly affected the final results by increasing the sampling in discontinuous regions when applying PINNs.[11] Traditional PINNs mostly use random or uniform sampling, which suffers from a critical drawback: sampling points may be concentrated in regions where physical constraints are already satisfied and the inherent error is small, whereas sparse sampling occurs in high-error regions. This causes a waste of computational resources in the low-value regions, whereas the accuracy in the high-value regions is insufficient. Optimizing the selection of internal collocation points can improve PINN training accuracy.

Numerous residual-based adaptive sampling schemes have been proposed in recent years to identify key regions within the solution domain using partial differential equation (PDE) residuals and allocate more sampling points to high-error regions where the solution exhibits high uncertainty or is difficult to fit accurately. Examples include residual-adaptive refinement (RAR),[12] residual-adaptive distribution, and residual-adaptive refinement with distribution,[13] and the failure-informed PINN method, which defines the failure probability based on residuals.[14] These adaptive sampling schemes allow the neural network to focus on critical regions during training, thereby improving the numerical solution accuracy of PDEs. However, these residual-based adaptive sampling algorithms typically adjust sampling dynamically based on the residual conditions throughout the training process of PINNs, requiring continuous iterative improvement. For instance, the RAR method adds the points with the largest

*Corresponding author. Email: ychen@sei.ecnu.edu.cn
© 2026 Chinese Physical Society and IOP Publishing Ltd. All rights, including for text and data mining, AI training, and similar technologies, are reserved.

PDE residuals to the existing collocation point set in each resampling phase. This continuous addition of sampling points inevitably results in a steady increase in the computational cost. Furthermore, most adaptive-sampling PINN algorithms primarily use a global perspective, aiming to continuously optimize the sampling distribution by adjusting the sampling points based on the residual conditions. However, they struggled to achieve significant accuracy improvements in key regions of complex solutions, such as areas with abrupt waveform changes or sharp gradients.

In this study, we propose a high-residual region resampling PINN (HRR-PINN) method to solve complex solutions, and apply it to the second-type derivative nonlinear Schrödinger (DNLSII). The DNLSII [15] equation

$$\mathrm{i}q_t + q_{xx} + \mathrm{i}|q|^2 q_x = 0, \tag{1}$$

is also known as the Chen-Lee-Liu equation. The DNLSII equation is used to simulate the propagation of self-steepening optical pulses without self-phase modulation. The research on this equation is increasing owing to its increasingly prominent physical relevance and the existing exploration space in obtaining new solutions that are not generated by gauge transformations between other derivative type nonlinear Schrödinger equations. [16–19] In Ref. [20], the soliton and rational solutions of the DNLSII equation were derived using the Wronskian technique. In addition, the Hirota bilinear method was used to obtain an N-soliton solution of the DNLSII equation. [21] Reference [22] explored the generalized Darboux transformation (DT) and rational soliton solutions of the DNLSII equation. In Ref. [23], rogue waves emerging on a plane-wave background of the DNLSII equation were studied using n-fold DT. In Ref. [24], the rogue wave on the periodic background for the DNLSII equation was obtained using odd-th order DT, and a PINN was applied to research the data-driven rogue wave on the periodic background of DNLSII equation.

To provide a controllable and abundant sample space for the HRR-PINN methods in this study, we first propose a concise form of general semi-degenerate DT for the DNLSII equation. Through this transformation, a wealth of exact localized wave solutions for the DNLSII equation can be obtained, including multiperiodic solutions and higher-order rogue wave solutions for multiperiodic backgrounds. The pretraining phase of the HRR-PINN method focuses on global modeling, whereas the secondary training phase specializes in optimizing high-error regions. By adjusting the sampling based on the global results of the initial training, the method effectively avoids the accumulation of early sampling biases in single-stage approaches, resulting in more accurate sampling optimization and more stable model convergence. The HRR-PINN method does not simply increase the number of sampling points. Instead, after identifying high-error regions, it supplements new sampling points in these regions while removing low-value points with the smallest residuals from the original sampling set. This maintains a stable total number of sampling points, thereby optimizing the distribution of sampling points and controlling computational costs. This optimization approach focuses on targeted improvements in critical high-error regions, with the primary goal of achieving significant accuracy improvements in key regions of complex solutions (e.g., areas with abrupt waveform changes or sharp gradients). Numerical experiments demonstrate that the proposed method significantly reduces the prediction errors when solving single-periodic solutions, rogue wave solutions on single-periodic backgrounds, and double-periodic solutions of the DNLSII equation, which verifies its effectiveness and generality.

2. N-Fold DT and Generalized Semi-Degenerate DT. The DNLSII equation (1) is derived from the following compatibility condition under the reduction condition $r = -q^*$ and the corresponding Lax pair is given as follows: [18]

$$\Psi_x = U\Psi, \quad \Psi_t = V\Psi, \tag{2}$$

where

$$\begin{aligned}
&\Psi(x,t,\lambda) = \begin{pmatrix} \phi(x,t,\lambda) \\ \varphi(x,t,\lambda) \end{pmatrix}, \\
&U = \left(-\mathrm{i}\lambda^2 - \frac{\mathrm{i}}{4}qr\right)\sigma_3 + \lambda Q, \\
&V = \left(-2\mathrm{i}\lambda^4 - \mathrm{i}qr\lambda^2 - \frac{1}{4}(qr_x - rq_x) - \frac{\mathrm{i}}{8}q^2r^2\right)\sigma_3 \\
&\qquad +2\lambda^3 Q + \lambda P, \\
&\sigma_3 = \begin{pmatrix} 1 & 0 \\ 0 & -1 \end{pmatrix}, \quad Q = \begin{pmatrix} 0 & q \\ r & 0 \end{pmatrix}, \\
&P = \begin{pmatrix} 0 & \mathrm{i}q_x + \frac{1}{2}q^2 r \\ -\mathrm{i}r_x + \frac{1}{2}r^2 q & 0 \end{pmatrix}.
\end{aligned}$$

Consider the gauge transformation $\Psi[N] = T\Psi$, where the transformation matrix T has the following the form:

$$T = \sum_{\ell=0}^{[\frac{N}{2}]} \begin{pmatrix} a_{N-2\ell}\lambda^{N-2\ell} & b_{N-2\ell-1}\lambda^{N-2\ell-1} \\ c_{N-2\ell-1}\lambda^{N-2\ell-1} & d_{N-2\ell}\lambda^{N-2\ell} \end{pmatrix},$$

where $[N/2]$ denotes the least integer function and a_0, b_0, c_0 and d_0 are constants. Specifically, any element of matrix T with a negative subscript is set to zero, whereas all other entries of matrix T depend on the variables x and t. Under this transformation, the Lax pair given by Eq. (2) is converted to

$$\Psi[N]_x = U[N]\Psi[N], \quad \Psi[N]_t = V[N]\Psi[N], \tag{3}$$

where $U[N] = U|_{q\to q[N], r\to r[N]}$, $V[N] = V|_{q\to q[N], r\to r[N]}$, and $(q[N], r[N])$ represent a new solution to Eq. (1).

Furthermore, considering the key problems associated with $T|_{\lambda=\lambda_j}\Psi(x,t,\lambda_j) = 0$, $j = 1, 2, \ldots, N$, and using Cramer's rule, the N-fold DT formula for the DNLSII equation is derived. Subsequently, considering the mixed higher-order spectral problem below, the generalized semi-degenerate DT can be derived from the N-fold DT formula using Taylor expansion and determinant calculations.

Theorem 2.1 (Generalized semi-degenerate DT formula): *Let*

$$\lambda_j \to \begin{cases} \lambda_1, & j_0 < j \in \text{odd} \le j_1 - 1, \\ \lambda_2, & j_0 < j \in \text{even} \le j_1, \\ \lambda_3, & j_1 < j \in \text{odd} \le j_2 - 1, \\ \lambda_4, & j_1 < j \in \text{even} \le j_2, \\ \ldots & \ldots \\ \lambda_{2m-1}, & j_{\hbar-1} < j \in \text{odd} \le j_\hbar - 1, \\ \lambda_{2m}, & j_{\hbar-1} < j \in \text{even} \le j_\hbar, \end{cases} \qquad j_0 = 2m \text{ and } j_\hbar = N - n.$$

The specific form of the new solution q_N is expressed as follows:

$$q^{[N]} = \begin{cases} \frac{|\widehat{W'}_N|}{|W'_N|} q - 2\mathrm{i}\frac{|M'_N|}{|W'_N|} & N \in \text{even}, \\ H\left(\frac{|\widehat{W'}_N|}{|W'_N|} q - 2\mathrm{i}\frac{|M'_N|}{|W'_N|}\right) & N \in \text{odd}, \end{cases} \tag{4}$$

where

$$H = \exp\left(\int_{(x_0,t_0)}^{(x,t)} \frac{1}{2}\mathrm{i}qr\mathrm{d}x - \frac{1}{4}\left(\mathrm{i}q^2r^2 - 2qr_x + 2rq_x\right)\mathrm{d}t\right),$$

$$W'_N = \begin{cases} (W'_{jk}),\ 1 \le j \le N-n, 1 \le k \le N, \\ (W_{jk}),\ N-n < j \le N, 1 \le k \le N, \end{cases}$$

$$M'_N = \begin{cases} (M'_{jk}),\ 1 \le j \le N-n, 1 \le k \le N, \\ (M_{jk}),\ N-n < j \le N, 1 \le k \le N, \end{cases}$$

$$\widehat{W'_N} = \begin{cases} (\widehat{W'_{jk}}),\ 1 \le j \le N-n, 1 \le k \le N, \\ (\widehat{W_{jk}}),\ N-n < j \le N, 1 \le k \le N, \end{cases}$$

$$W_{jk} = \begin{cases} \lambda_j^{N-k}\varphi_j,\ k \in \text{odd}, \\ \lambda_j^{N-k}\phi_j,\ k \in \text{even}, \end{cases}$$

$$M_{jk} = \begin{cases} \lambda_j^{N}\phi_j, & k = 1, \\ \lambda_j^{N-k}\varphi_j,\ k \in \text{even} \ge 2, \\ \lambda_j^{N-k}\phi_j,\ k \in \text{odd}, \end{cases} \tag{5}$$

$$\widehat{W}_{jk} = \begin{cases} \lambda_j^{N-k}\phi_j,\ k \in \text{odd}, \\ \lambda_j^{N-k}\varphi_j,\ k \in \text{even}, \end{cases}$$

$$W'_{jk} = \lim_{\epsilon\to 0} \frac{\partial^{n_j} W_{jk}(\lambda_j + \epsilon)}{n_j!\partial\epsilon^{n_j}},$$

$$M'_{jk} = \lim_{\epsilon\to 0} \frac{\partial^{n_j} M_{jk}(\lambda_j + \epsilon)}{n_j!\partial\epsilon^{n_j}},$$

$$\widehat{W'_{jk}} = \lim_{\epsilon\to 0} \frac{\partial^{n_j} \widehat{W_{jk}}(\lambda_j + \epsilon)}{n_j!\partial\epsilon^{n_j}},$$

$$n_j = \begin{cases} 0, & j \le j_0, \\ \left[\frac{j - j_0 + 1}{2}\right], & j_0 < j \le j_1, \\ \left[\frac{j - j_1 + 1}{2}\right], & j_1 < j \le j_2, \\ \ldots \\ \left[\frac{j - j_{\hbar-1} + 1}{2}\right], & j_{\hbar-1} < j \le j_\hbar. \end{cases}$$

Remark 1 *Matrix elements are processed in distinct regions as required. Elements in the degenerate region (first $N-n$ rows) undergo Taylor expansions of varying orders, whereas elements in the non-degenerate region (last n rows) retain their original form. Specifically, when $n = N$, the generalized semi-degenerate DT formula is transformed into the N-fold DT formula.*

The seed solution of the Lax pair (2) is given by $r = -q^* = -c\mathrm{e}^{-\mathrm{i}(ax+bt)}$ with $b = -a^2 - c^2a$ (In this work, we set $a = -1$ and $c = 1$). By solving the Lax pair (2) and combining the symmetry conditions of the DNLSII equation,[23] we obtain the corresponding vector eigenfunctions Ψ_k associated with λ_k. Complex nonlinear wave solutions, such as multiperiodic solutions and high-order rogue wave solutions on a multiperiodic background, can then be generated using the semi-degenerate DT transform, which can provide a richer sample space for the HRR-PINN method. For example, when $n = N = 1$, $\lambda = \mathrm{i}\beta$, the exact single-periodic wave q_{p1} solution is derived. Similarly, for $n = N = 2$, $\lambda_1 = \mathrm{i}\beta_1$, and $\lambda_2 = \mathrm{i}\beta_2$, we obtain the double periodic wave solution q_{p2}. While considering $N = 3$, $n = 1$, with the spectral parameters specified as $\lambda_1 = (\sqrt{-2a}/2) + \mathrm{i}c/2 + \epsilon^2$, $\lambda_2 = -\sqrt{-2a}/2 + \mathrm{i}c/2 + \epsilon^2$, and $\lambda_3 = \mathrm{i}\beta_3$, the first-order rogue wave solution on single-periodic background q_{r1p1} is explicitly derived.

3. High-Residual Regions Resampling PINN Method. Consider the PDE with Dirichlet boundary conditions:

$$\begin{cases} q_t + \mathcal{N}_q(q, q_x, q_{xx}, q_{xxx}, \ldots) = 0, \\ q(\boldsymbol{x}, t_0) = q_0(\boldsymbol{x}),\ q(\boldsymbol{x}_\mathrm{B}, t) = B(\boldsymbol{x}, t), \\ \quad \boldsymbol{x} \in \Omega,\ \boldsymbol{x}_\mathrm{B} \in \partial\Omega,\ t \in [t_0, t_1], \end{cases} \tag{6}$$

where q denotes a complex-valued function of variables x and t, and $\mathcal{N}_q(q, q_x, q_{xx}, q_{xxx}, \ldots)$ denoes a nonlinear function of $q(x,t)$ and its arbitrary-order derivatives with respect to x. where $\boldsymbol{x} = (x_1, \ldots, x_N) \in \Omega$, $\partial\Omega$ denotes the boundary of Ω, $q = q(\boldsymbol{x}, t)$ denotes the solution function, and Ω represents a subset of $\mathbb{R}^N$.

Let $q(x,t) = u(x,t) + \mathrm{i}v(x,t)$, where the physical information terms in the neural network can be defined as follows:

$$\begin{aligned} f_u &= u_t + \mathcal{N}_u(u, u_x, u_{xx}, u_{xxx}, \ldots), \\ f_v &= v_t + \mathcal{N}_v(v, v_x, v_{xx}, v_{xxx}, \ldots). \end{aligned} \tag{7}$$

The specific process of HRR-PINN method is as follows.

Pre-Training Phase. First, a fully connected feed-forward neural network with depth d is constructed as $\boldsymbol{u}(\boldsymbol{x}^0; \bar{\Theta}) = \left(\mathcal{A}_d \circ \sigma \circ \mathcal{A}_{d-1} \circ \cdots \circ \sigma \circ \mathcal{A}_1\right)(\boldsymbol{x}^0)$, input layer

$\boldsymbol{x}^0 = (\boldsymbol{x}, t)$, $\bar{\Theta} = \{\boldsymbol{W}_i, \boldsymbol{b}_i\}_{i=1}^{d}$ represents the trainable parameters of the network, and the output $\boldsymbol{u}$ is used to approximate the solution of the problem. $\mathcal{A}_i = \mathcal{A}_i(\boldsymbol{x}_{i-1}) = \boldsymbol{W}_i\boldsymbol{x}_{i-1} + \boldsymbol{b}_i, \boldsymbol{x}_{i-1} \in \mathbb{R}^{N_{i-1}}, \boldsymbol{x}_i \in \mathbb{R}^{N_i}$, where N_i represent the number of neurons in the i-th hidden layer, σ represents a nonlinear activation function [consider $\sigma = \tanh(x)$ in this study], $\boldsymbol{W}_i \in \mathbb{R}^{N_{i-1}\times N_i}$ and $\boldsymbol{b}_i \in \mathbb{R}^{N_i}$ represent the network weights matrix and bias vector of the i-th layer, respectively.

The loss function is defined as follows: $\text{Loss} = \text{Loss}_u + \text{Loss}_v + \text{Loss}_{f_u} + \text{Loss}_{f_v}$, where

$$\text{Loss}_u = \frac{1}{N_q}\sum_{i=1}^{N_q}\left(|\hat{u}(x_i,t_i) - u(x_i,t_i)|^2\right),$$

$$\text{Loss}_v = \frac{1}{N_q}\sum_{i=1}^{N_q}\left(|\hat{v}(x_i,t_i) - v(x_i,t_i)|^2\right),$$

$$\text{Loss}_{f_u} = \frac{1}{N_f}\sum_{j=1}^{N_f}\left(|\hat{f}_u(x_j,t_j)|^2\right),$$

$$\text{Loss}_{f_v} = \frac{1}{N_f}\sum_{j=1}^{N_f}\left(|\hat{f}_v(x_j,t_j)|^2\right),$$

where N_q denotes the number of random sampling boundary points (x_i, t_i) and N_f denotes the number of internal collocation points (x_j, t_j) selected by Latin hypercube sampling (LHS). $\hat{u}(x_i, t_i)$ and $\hat{v}(x_i, t_i)$ and $u(x_i, t_i)$ and $v(x_i, t_i)$ are the predictions and exact values of DNLSII equations at boundary points, respectively. $\hat{f}_u(x_j, t_j)$ and $\hat{f}_v(x_j, t_j)$ represent the physical information at the internal collocation points. The optimization algorithm used in this study is the L-BFGS algorithm, and the training terminates when the loss function falls below a given threshold or when the specified maximum number of iterations is reached.

Locate a High-Error Area. By calculating the residual of the equation in the calculation domain based on pretraining, potential high-error regions with low satisfaction of physical constraints can be identified. The residual threshold (δ = 0–100%, where $\delta = 0$ corresponds to the traditional PINN) was determined using the quantile thresholding method, and the grid points with residual values exceeding the threshold were defined as the high residual region. Thus, the coordinates of the high-residual regions can be obtained. After determining the high-error regions, new sampling points were added to these regions to improve the learning ability of the model for these key regions.

Optimize Sampling Points. Randomly select N_{new} points from the high-residual regions as the new sampling points. To control the calculation cost and avoid a continuous increase in the total number of sampling points, the residuals of the original physical sampling points are sorted from small to large, and the N_{new} points with the smallest residuals and low information values are deleted from the original sampling set. At this point, the new sampling points are merged with the remaining original internal matching points. Thus, it not only ensures that there are enough sampling points in the high-error area to improve the accuracy but also ensures that the computing resources will not be wasted in those areas that contribute less to the improvement of model accuracy and realizes the efficient use of sampling points.

Secondary Training. At this stage, the model uses the new sampling point distribution to further learn the characteristics of the solutions of the PDE, particularly in the high-error region. Through secondary training, the model can capture the physical phenomena in key areas more accurately, improve the prediction accuracy in these areas, and obtain more accurate numerical solutions.

To measure the discrepancy between the predicted and true values of the model, we define the L_2 norm error

$$L_2 \text{ norm error} = \frac{\sqrt{\sum_{i=1}^{N}|q(x_i,t_i) - \hat{q}(x_i,t_i)|^2}}{\sqrt{\sum_{i=1}^{N}|\hat{q}(x_i,t_i)|^2}}.$$

The Xavier method was used for network initialization, and all codes in this study were based on Python 3.7 and TensorFlow 1.15. All numerical experiments were conducted on a DELL Precision 7920 Tower computer with a 2.10-GHz 8-core Xeon Silver 4110 processor, 64 GB of memory, and an 11-GB NVIDIA GeForce GTX 1080 Ti video card.

4. Data-Driven Solution of the DNLSII Equation. In this section, data-driven single-periodic waves, rogue waves on single-periodic backgrounds, and double-periodic waves for the DNLSII equation are learned using HRR-PINN. The physical information terms can be defined as follows:

$$\begin{aligned} f_u &= -v_t + u_{xx} - u^2 v_x - v^2 v_x, \\ f_v &= u_t + v_{xx} + u^2 u_x + v^2 u_x. \end{aligned} \tag{8}$$

In the following, the spatial domain $\Omega = [x_0, x_1]$ is discretized into 513 points and the time domain $[t_0, t_1]$ is discretized into 601 points using the traditional finite difference method.

4.1. Data-Driven Single-Periodic Wave. By setting $\beta = 1/2$, $x_0 = -6$, $x_1 = 6$, $t_0 = -1$, $t_1 = 1$, $N_q = 100$, and $N_f = 10000$, a training dataset for pre-training is generated. The point selection for pre-training is shown in Fig. 1(a). After 14860 iterations, the L_2-norm error of the predicted solution was 9.202286×10^{-3} using a traditional PINN with a 9-layer neural network, where each layer had 40 neurons. Subsequently, considering $\delta = 10\%, N_{\text{new}} = 1000$, the remaining original sampling points were merged with the newly added sampling points. The point selection for resampling based on the PDE residuals is shown in Fig. 1(b). The blue point represents the remaining points with pre-training, and the red points represent the new points in the secondary training in Fig. 1.

With the neural network structure in pretraining, the model was retrained based on this optimized sampling set. After 10708 iterations, the L_2 norm error of the predicted solution reached 4.869479×10^{-3} using HRR-PINN. Figure 2(a) shows a comprehensive comparison between the

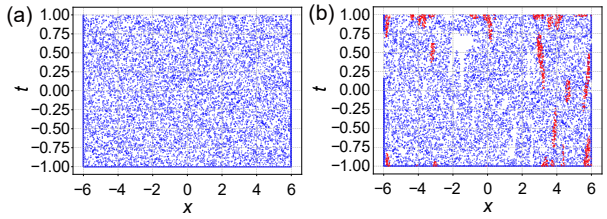

Fig. 1. (a) Distribution of collocation points in PINN method. (b) Distribution of collocation points in HRR-PINN method.

predicted values obtained using the HRR-PINN and exact values. The 3D plot of the data-driven single periodic wave of the DNLSII equation is shown in Fig. 2(b).

The errors of the traditional PINN were 9.202286×10^{-3}, whereas for $\delta = 5\%$, 10%, 15%, and 20%, the HRR-PINN method achieved significantly lower errors of 8.429815×10^{-3}, 4.869479×10^{-3}, 5.218842×10^{-3}, and 5.401567×10^{-3} [see Fig. 3(a)], respectively. When N_f was set to 8000, 10000, and 12000, the errors obtained using the PINN method were 5.319548×10^{-3}, 9.202286×10^{-3}, and 7.432158×10^{-3}. For $N_f = 10000$, the error of HRR-PINN with $\delta = 10\%$ was 4.869479×10^{-3}. For $N_f = 12000$, the error of the HRR-PINN method with $\delta = 5\%$ was 3.510761×10^{-3}. Although there was a slight increase in error in the HRR-PINN method when $N_f = 8000$, the experimental results showed that the high residual area resampling PINN method accurately located high error areas and optimized the sampling points, significantly improving the accuracy of the single-period solutions. More intuitively, see Fig. 3(b).

4.2. Data-Driven Rogue Wave on the Single-Periodic Background. Considering $\beta_3 = -0.02$, $x_0 = -9$, $x_1 = 9$, $t_0 = -1.5$, $t_1 = 1.5$, $N_q = 600$, and $N_f = 10000$, using a 9-layer PINN with 60 neurons per layer, the L_2 norm error of the predicted solution was 1.486246×10^{-2} by pre-training after 20815 iterations. The point selection for pre-training is shown in Fig. 4(a). By choosing $\delta = 5\%$ and $N_{\text{new}} = 1000$, the point selection of resampling based on pretraining is shown in Fig. 4(b).

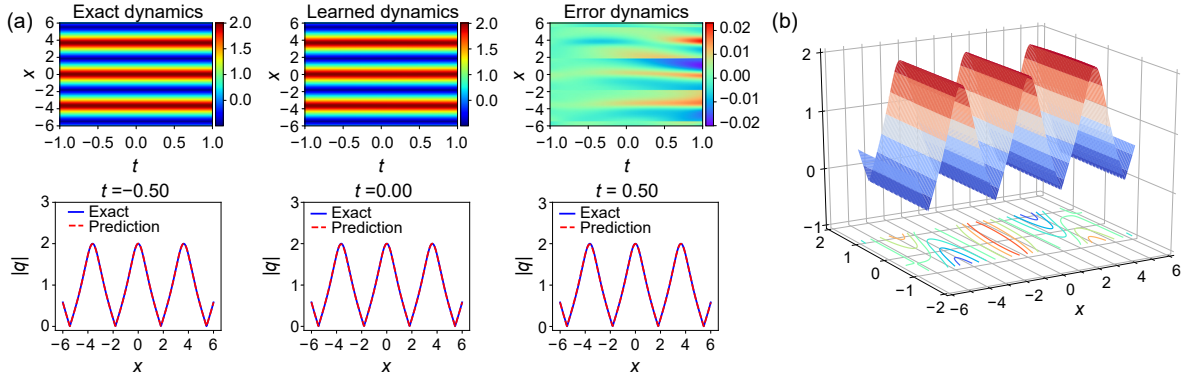

Fig. 2. (a) The upper part of the figure shows the density map to compare the exact solutions and predicted solutions of the DNLSII equations and the errors between them; the lower part shows a time slice. (b) 3D plot of the data-driven single-periodic wave of the DNLSII equation.

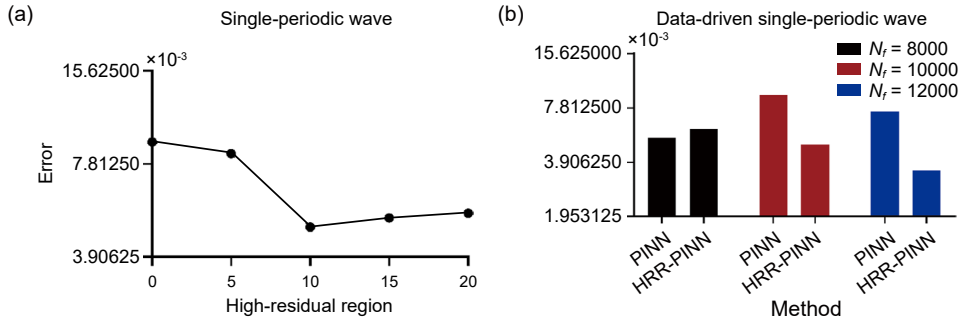

Fig. 3. (a) Error of data-driven single-periodic wave using HRR-PINN method with different high-residual regions. (b) Error of data-driven single-periodic wave using PINN and HRR-PINN methods with different internal collocation points.

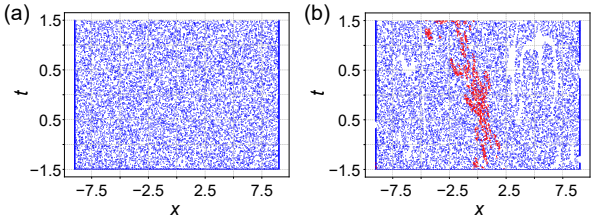

Fig. 4. (a) Distribution of collocation points in PINN. (b) Distribution of collocation points in the HRR-PINN method.

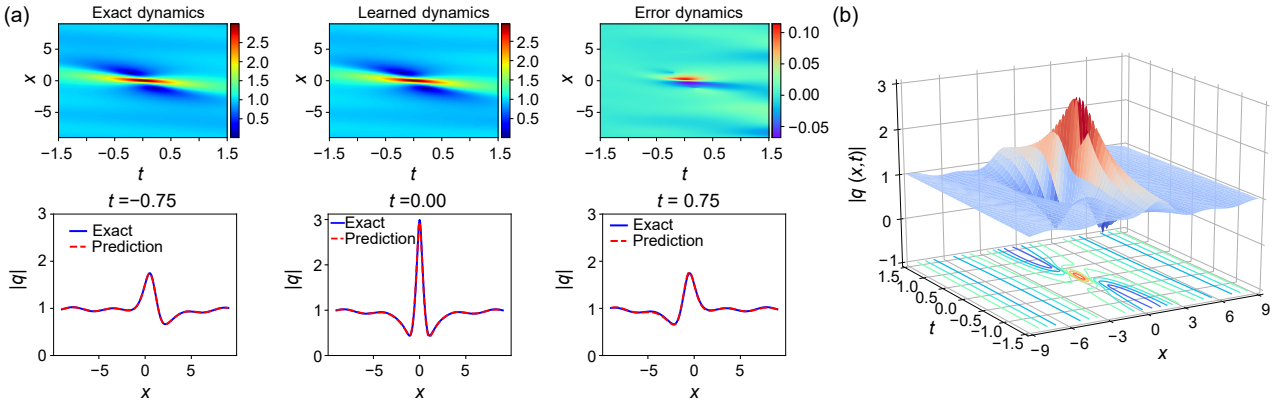

Fig. 5. (a) The upper part of the figure shows the density map to compare the exact solutions and predicted solutions of the DNLSII equations, and the errors between them; the lower part shows a time slice. (b) 3D plot of the data-driven rogue waves on a single-periodic background of the DNLSII equation.

After 23102 iterations, the L_2 norm error of the predicted solution reached 9.333405×10^{-3} using the HRR-PINN method. Figure 5 shows the numerical results for a data-driven rogue wave on a single-periodic background using the HRR-PINN algorithm.

Considering $N_q = 600$, the errors of the traditional PINN were 5.78×10^{-2}, 1.486246×10^{-2}, and 1.30081×10^{-2} for internal collocation points $N_f = 8000$, 10000, and 12000, respectively. For the HRR-PINN method, the corresponding errors were 6.665292×10^{-3} ($\delta = 25\%$), 7.8125×10^{-3} ($\delta = 30\%$), and 1.180864×10^{-2} ($\delta = 5\%$), as shown in Fig. 6.

4.3. Data-Driven Double-Periodic Wave of the DNLSII Equation. Considering $\beta_1 = 1/2$, $\beta_2 = 2/3$, $x_0 = -6$, $x_1 = 2$, $t_0 = -2$, $t_1 = 1$, $N_q = 400$, and $N_f = 12000$, using a 9-layer PINN with 60 neurons per layer, the L_2 norm error of the predicted solution was 3.240103×10^{-2} by pre-training after 16956 iterations. The point selection for pre-training is shown in Fig. 7(a). We set $\delta = 5\%$, $N_{\text{new}} = 1000$, and the point selection of resampling based on the PDE residuals is shown in Fig. 7(b).

After 19497 iterations, the L_2 norm error reached 1.857115×10^{-2}. The training results of the double-periodic wave using HRR-PINN are shown in Fig. 8.

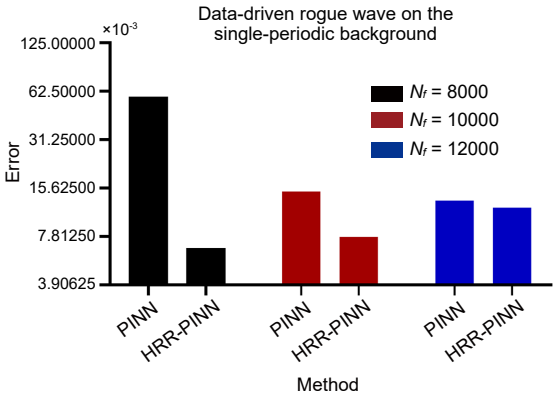

Fig. 6. Error of data-driven rogue wave on the single-periodic background using PINN and HRR-PINN methods with different internal collocation points.

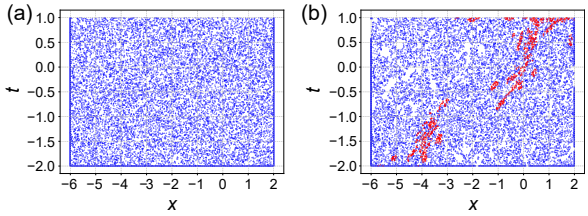

Fig. 7. (a) Distribution of collocation points using the PINN method. (b) Distribution of collocation points using the HRR-PINN method.

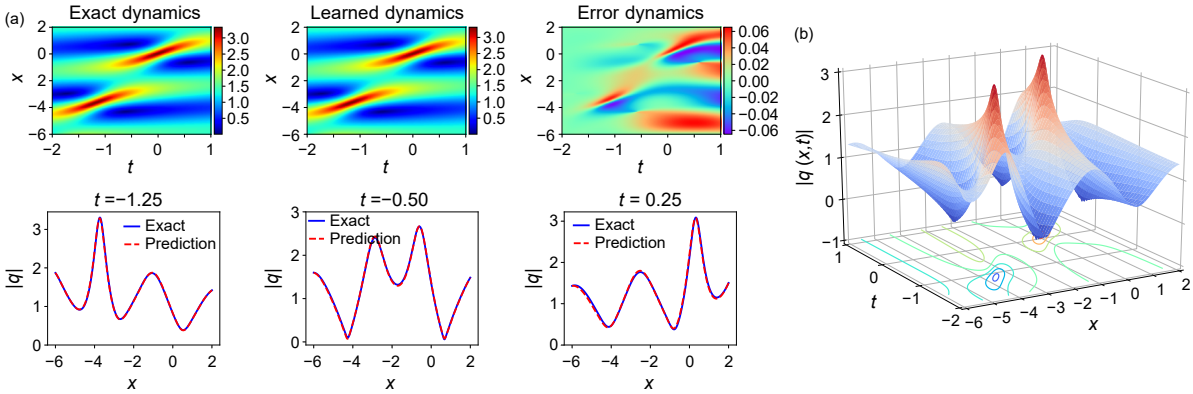

Fig. 8. (a) The upper part of the figure shows the density map to compare the exact and predicted solutions of the DNLSII equations and the errors between them; the lower part shows a time slice. (b) 3D plot of the data-driven double-periodic wave of the DNLSII equation.

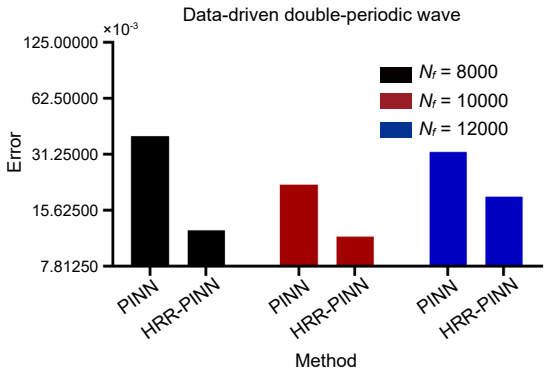

Fig. 9. Error of data-driven double-periodicity using PINN and HRR-PINN methods with different internal collocation points.

Table 1. Relative errors and reduction rates of PINN and HRR-PINN methods under different internal collocation points N_f.

Wave type	RER under N_f		
	8000	10000	12000
Single-periodic	−11.95%	47.08%↓	52.76%↓
Rogue-periodic	88.47%↓	47.43%↓	9.22%↓
Double-periodic	68.86%↓	47.70%↓	42.68%↓

When N_f was set to 8000, 10000, and 12000, the prediction errors of the traditional PINN method were 3.909731×10^{-2}, 2.159723×10^{-2}, and 3.240103×10^{-2}, respectively. After using the HRR-PINN method with $\delta = 5\%$, the corresponding errors were reduced to 1.21727×10^{-2}, 1.129466×10^{-2}, and 1.857115×10^{-2} for the same N_f values, as shown in Fig. 9.

To better compare the generalization abilities of HRR-PINN and PINN methods, we defined the relative error reduction rate (RER) as $\mathrm{RER} = \left[\frac{\mathrm{PINN_{error}}-\mathrm{HRR\text{-}PINN_{error}}}{\mathrm{PINN_{error}}}\right]\times 100\%$. Based on the numerical results above, we summarized the RER of HRR-PINN and PINN methods in Table 1.

As listed in Table 1, the HRR-PINN method significantly outperformed the traditional PINN method. This advantage holds across the single-periodic, rogue-periodic, double-periodic, and various numbers of internal collocation points ($N_f = 8000, 10000, 12000$). Only in the case of a single-periodic wave with $N_f = 8000$ HRR-PINN exhibited a slight increase in error (RER = −11.95%). In all the other scenarios, a substantial error reduction was achieved. The maximum RER reached 88.47% for rogue-periodic waves at $N_f = 8000$. For single- and double-periodic waves with $N_f = 10000$ and 12000, respectively, the RER consistently exceeded 42%. These results demonstrate its superiority in improving the prediction accuracy, stability, and generalization ability of PINNs.

5. Conclusions and Discussions. In this study, we developed an HRR-PINN method to solve complex solutions, which were validated using the DNLSII equation. We derived a general semi-degenerate Darboux transformation for the DNLSII equation, generating diverse exact complex localized wave solutions that provided a rich dataset for the HRR-PINN. HRR-PINN introduces a two-stage training paradigm that uses the pre-training model to make predictions and obtain the residual values of the PDE over the entire computational domain and then constructs an optimized sampling set that adds points in high-error regions while removing low-residual points, maintaining a constant sample size to control costs. The numerical results show that the HRR-PINN method substantially outperforms the traditional PINN under various wave types and collocation point numbers, achieving a remarkable error reduction in nearly all cases, thus demonstrating its clear superiority in improving the prediction accuracy, stability, and generalization of PINNs. HRR-PINN demonstrated superior performance for the DNLSII equation and generality for other PDEs with complex solutions. Future study will validate HRR-PINN on other nonlinear PDEs such as variable-coefficient NLS and coupled systems. HRR-PINN provides an efficient approach for complex nonlinear wave systems with applications in oceanography, optics, and related fields.

Acknowledgements. This project was supported by the National Natural Science Foundation of China (Grant Nos. 12547136, 12575002, and 12235007).

References

[1] Raissi M, Perdikaris P, and Karniadakis G E 2019 *J. Comput. Phys.* **378** 686
[2] Lin S N and Chen Y 2022 *J. Comput. Phys.* **457** 111053
[3] Pu J C and Chen Y 2024 *J. Comput. Phys.* **510** 113090
[4] Lin Z and Chen Y 2025 *J. Comput. Phys.* **539** 114243
[5] Tian S F, Niu Z J, and Li B 2023 *Nonlinear Dyn.* **111** 16467
[6] Wu G Z, Fang Y, Wang Y Y, Wu G C, and Dai C Q 2021 *Chaos, Soliton. Fract.* **152** 111393
[7] Zhang Z Y, Liu M W, Xing X W, Zhang S Z, Yan Z Y, and Liu W J 2025 *Comput. Method. Appl. M.* **438** 117852
[8] Tian S F, Yu Y X, and Li B 2025 *Chin. Phys. Lett.* **42** 120001
[9] Zhou H S, Zhang Z Y, liu M W, Qi F H, and Liu W J 2025 *Chin. Phys. Lett.* **42** 070001
[10] Tian S F, Li B, and Zhang Z 2024 *Chin. Phys. Lett.* **41** 030201
[11] Mao Z, Jagtap A D, and Karniadakis G E 2020 *Comput. Method. Appl. M.* **360** 112789
[12] Lu Z P and Karniadakis G E 2021 *SIAM Rev.* **63** 208
[13] Wu C, Zhu M, Tan Q, Kartha Y, and Lu L 2023 *Comput. Method. Appl. M.* **403** 115671
[14] Gao Z, Yan L, and Zhou T 2023 *SIAM J. Sci. Comput.* **45** A1971
[15] Chen H H, Lee Y C, and Liu C S 1979 *Phys. Scr.* **20** 490
[16] Xu S W, He J S, and Wang L H 2011 *J. Phys. A: Math. Gen.* **44** 305203
[17] Moses J, Malomed B A, and Wise F W 2007 *Phys. Rev. A* **76** 021802
[18] Wadati M and Sogo K 1983 *J. Phys. Soc. Jpn.* **52** 394
[19] Gerdjikov V S and Ivanov I 1983 *J. Phys. Bulg.* **10** 130
[20] Zhai W and Chen D Y 2008 *Phys. Lett. A* **372** 4217
[21] Zhai W and Chen D Y 2008 *Commun. Theor. Phys.* **49** 1101
[22] Yang B, Zhang W G, Zhang H Q, and Pei S B 2014 *Appl. Math. Comput.* **242** 863
[23] Zhang Y S, Guo L J, He J S, and Zhou Z X 2015 *Lett. Math. Phys.* **105** 853
[24] Peng W Q, Pu J C, and Chen Y 2022 *Commun. Nonlinear Sci.* **105** 106067